AIP Journal of Applied Physics

Model-independent measurement of the charge density distribution along an Fe atom probe needle using off-axis electron holography without mean inner potential effects

V. Migunov, A. London, M. Farle, and R. E. Dunin-Borkowski

Citation: Journal of Applied Physics **117**, 134301 (2015); doi: 10.1063/1.4916609
View online: http://dx.doi.org/10.1063/1.4916609
View Table of Contents: http://scitation.aip.org/content/aip/journal/jap/117/13?ver=pdfcov
Published by the AIP Publishing

Model-independent measurement of the charge density distribution along an Fe atom probe needle using off-axis electron holography without mean inner potential effects

V. Migunov,[1,a)] A. London,[2] M. Farle,[3] and R. E. Dunin-Borkowski[1]
[1]*Ernst Ruska-Centre for Microscopy and Spectroscopy with Electrons (ER-C) and Peter Grünberg Institute (PGI), Forschungszentrum Jülich, D-52425 Jülich, Germany*
[2]*Department of Materials, University of Oxford, Parks Road, Oxford OX1 3PH, United Kingdom*
[3]*Fakultät für Physik and Center of Nanointegration (CeNIDE), Universität Duisburg-Essen, D-47048 Duisburg, Germany*

(Received 7 November 2014; accepted 20 March 2015; published online 1 April 2015)

The one-dimensional charge density distribution along an electrically biased Fe atom probe needle is measured using a model-independent approach based on off-axis electron holography in the transmission electron microscope. Both the mean inner potential and the magnetic contribution to the phase shift are subtracted by taking differences between electron-optical phase images recorded with different voltages applied to the needle. The measured one-dimensional charge density distribution along the needle is compared with a similar result obtained using model-based fitting of the phase shift surrounding the needle. On the assumption of cylindrical symmetry, it is then used to infer the three-dimensional electric field and electrostatic potential around the needle with ~10 nm spatial resolution, without needing to consider either the influence of the perturbed reference wave or the extension of the projected potential outside the field of view of the electron hologram. The present study illustrates how a model-independent approach can be used to measure local variations in charge density in a material using electron holography in the presence of additional contributions to the phase, such as those arising from changes in mean inner potential and specimen thickness.
 [http://dx.doi.org/10.1063/1.4916609]

I. INTRODUCTION

The ability to measure local variations in charge density, electric field, and electrostatic potential in nanoscale materials and devices, such as doped semiconductors[1–4] and nanoscale field emitters,[5–8] in the transmission electron microscope (TEM) is important for understanding the relationship between internal microstructure, chemistry, defects, and functional properties.

Here, we show how the TEM technique of off-axis electron holography can be used to quantify the charge density distribution in an Fe needle that was prepared for examination using atom probe tomography (APT). The latter technique involves the atom-by-atom field evaporation of a material by an applied voltage, in order to provide a time-of-flight mass spectrum and the position of each atom in the tip.[9,10] Although the influence of the shape, crystallography and chemical composition of an APT needle on ion trajectories[11] can be simulated numerically[12] and models of the dielectric properties of embedded nanoparticles can be fitted to experimental measurements,[13] the development of a technique that can be used to measure the electric field around such a needle, or equivalently the charge distribution within it, promises to provide a more direct method for minimising artefacts in the reconstructed volume.[10]

Off-axis electron holography provides direct access to the phase shift

$$\phi(x,y) = C_E \int V(x,y,z)dz - \frac{e}{\hbar}\int A_z(x,y,z)dz, \qquad (1)$$

of the high-energy electron wave that has passed through an electron-transparent specimen in the TEM. In Eq. (1), C_E is a constant that depends on the microscope accelerating voltage and takes a value of 6.53×10^6 rad V^{-1} m^{-1} at 300 kV, while V and A_z are the electrostatic potential and the component of the magnetic vector potential in the electron beam direction z, respectively.[14–16]

Recently, Beleggia *et al.*[17] showed that the magnitude and direction of the electric field around the tip of an electrically biased ellipsoidal metallic needle can be measured by fitting simulations based on *theoretical models* for the charge density distribution along the needle to electron holographic phase images or Lorentz micrographs. Here, we use a *model-independent* approach[18] to determine the charge density distribution along an electrically biased Fe APT needle directly from recorded phase images. A key advantage of the present approach, which is based on integration of the Laplacian of the phase or, equivalently, contour integration of the gradient of the phase, is that it is insensitive to perturbation of the vacuum reference wave used to generate the hologram by the electromagnetic field of the specimen itself,[19] so long as the region from which the reference wave is obtained is itself charge-free.[20–22] However, in the past, it has suffered from an important limitation resulting from the effect of the mean inner potential contribution to the phase shift on the measured charge density distribution.[23] We show that this limitation can be overcome by analysing the *difference* between

[a)]Electronic mail: v.migunov@fz-juelich.de

electron holographic phase images acquired with different voltages applied to the specimen.[24] We compare our results with model-based fitting of an analytical simulation to the measured phase difference outside the same needle,[17,25] which requires the perturbed reference wave to be taken into account. We find that the projected charge density within the needle is almost constant along its length, with the model-independent approach providing evidence for the presence of charge accumulation at the tip of the needle. On the assumption of cylindrical symmetry (which is supported by the acquisition of a tilt series of electron holograms), the measured charge density distribution is used to infer the three-dimensional electric field and electrostatic potential around the end of the needle, without needing to consider either the influence of the perturbed reference wave or the extension of the projected potential outside the field of view of the electron hologram. Our results provide a step towards developing an approach that could be used to measure the electric field around a needle-shaped specimen during an APT experiment.[26] They are also relevant for the interpretation of similar results obtained from needle-shaped specimens using other phase contrast techniques, including in-line electron holography,[27–29] ptychography,[30] diffractive imaging and differential phase contrast microscopy.[31]

II. EXPERIMENTAL DETAILS

High-purity powders of Fe and Y_2O_3 with a target composition of Fe-0.3 wt. % Y_2O_3 (Alfa Aesar, Johnson Matthey group, London) were mechanically alloyed by ball milling in an Ar atmosphere for 4 h at 1000 rpm with a ball to powder ratio of 10:1. The mechanically alloyed powder was consolidated by hot extrusion at 1050 °C, annealed at 950 °C for 2 h, and air-cooled. 0.5-mm-thick disks were cut from the resulting 12-mm-diameter rod. Matchsticks with square cross-sections were cut from these disks. Needles with tip radii of 50–100 nm were then produced by electropolishing in two stages: first by using 25% perchloric acid in 75% acetic acid and then by using 2% perchloric acid in methanol.[9]

A single Fe APT needle containing Y_2O_3 particles was examined under an applied electrical bias using a scanning tunnelling microscopy (STM)-TEM specimen holder from Nanofactory Instruments[32] in an FEI Titan 80-300 TEM operated at 300 kV. The needle was mounted on the fixed side of the holder, while an electrochemically sharpened counter-electrode made from 0.25-mm-diameter W wire that had been etched in a solution of KOH to an apex radius of approximately 50–100 nm was placed on the moveable side. The counter-electrode was initially brought into contact with the needle to ensure that they were at the same height. The distance between the electrodes was then set to approximately 1 μm, as shown in Fig. 1.

Off-axis electron holograms of the end of the needle were acquired using 8 s exposure times with an interference fringe spacing of 3.4 nm (7.3 pixels), resulting in a spatial resolution in reconstructed phase images of approximately 10 nm. Holograms were recorded from the area shown in Fig. 1(b) at different specimen tilt angles over a range of

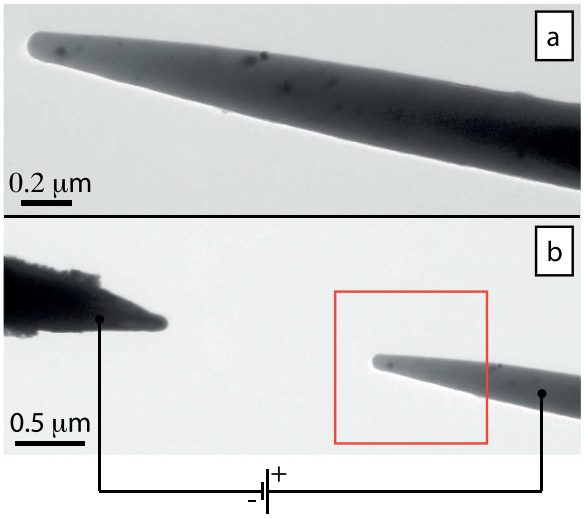

FIG. 1. (a) Bright-field TEM image showing the Fe APT needle containing Y_2O_3 particles. (b) Bright-field TEM image of the APT needle (right) and the W counter-electrode (left), with the scheme of the electrical circuit used in the experiment overlaid. The red box shows the approximate area from which electron holograms were acquired.

$\pm 45°$ (with the tilt axis parallel to the axis of the needle), with 6 different voltages of 0, 5, 10, 20, 30, and 40 V applied between the needle and the counter-electrode. A representative electron hologram is shown in the supplementary material.[33] Vacuum reference electron holograms were recorded from a region of vacuum far from the needle. Reconstruction of holograms was carried out using a standard fast Fourier-transform-based method.[34] Subtraction of the mean inner potential and magnetic contribution to the phase was achieved by using the object wave recorded at 0 V bias as a reference wave for holograms acquired at all other voltages. No further processing, smoothing, or interpolation of the resulting phase images was performed before making measurements of the projected charge density in the needle.

III. MEASUREMENT OF CHARGE DENSITY

A. Model-independent approach

Model-independent measurement of the charge Q, projected in the electron beam direction, from a recorded electron-optical phase image, can be performed by contour integration of the phase gradient according to the expression

$$Q = -\frac{\epsilon_0}{C_E}\oint_C \{\nabla_{\mathbf{R}}\phi(\mathbf{r}(s))\}\cdot\mathbf{n}(\mathbf{r}(s))ds, \qquad (2)$$

where ϵ_0 is the permittivity of free space, $\mathbf{r}$ is a two-dimensional vector in the plane of the image, and $\mathbf{n}$ is the outward normal vector to a section s of the integration contour C.[18,23] In the analysis presented below, we used rectangular integration contours aligned parallel to x and y to integrate the y and x components of the phase gradient, respectively. Evaluation of phase derivatives was performed directly from complex image waves without phase unwrapping.

The primary advantages of the model-independent approach for measuring the total charge within an integration contour are that it is applicable to specimens of arbitrary

geometry, requires only a basic knowledge of the likely positions of the charged objects within the field of view and, according to Eq. (2), is insensitive to the perturbed reference wave so long as it does not itself enclose any charge. The primary disadvantage of the model-independent approach is that, for a specimen whose thickness and/or composition changes across the field of view, such as an APT needle, the measured charge distribution can be affected by the mean inner potential contribution to the recorded phase shift, as a result of the presence of effective local dipoles on the specimen surface.[35] (If the needle had a constant specimen thickness profile along its length, then the use of the model-independent approach to measure the charge density along its length would not be influenced by the mean inner potential, as each contour integral would contain zero net charge arising from the effective surface dipoles. It is precisely because a needle has a changing specimen thickness profile that the effective surface dipoles do not cancel each other out in each contour integral, apart from special situations, such as when the contour encloses the entire object). Local changes in dynamical diffraction can also introduce artefacts for a similar reason.

In order to illustrate the nature of this problem, Fig. 2 shows a simulated phase image of a needle-shaped specimen that has an ellipsoidal three-dimensional shape and a constant charge density of $\sigma = 1.37\,\bar{e}/\mathrm{nm}$ along its length (see below). The mean inner potential contribution to the phase is localised inside the needle, while the charge is responsible for an additional variation in phase both inside and outside its edge. The cumulative (integrated) charge along the needle was measured, using the approach described by Eq. (2), by shrinking the indicated integration contour in the direction marked by an arrow. In the graph shown in Fig. 2, the red line shows the input cumulative charge along the needle, while the black profile shows the result of applying Eq. (2) to measure the cumulative charge along the needle from the simulated phase image, including the contribution from the mean inner potential. The black profile shows a significant step at the edge of the specimen and a strong discrepancy with respect to the input charge profile, highlighting the fact that for the present specimen subtraction of the mean inner potential contribution to the phase is essential for successful measurement of the charge using the model-independent contour integration method. A further issue is that, as the approach makes use of contour integration of the phase gradient, it is very sensitive to noise. Smoothing or averaging approaches can be used, but can result in degradation of resolution and artefacts. This point and other artefacts associated with the mean inner potential and magnetic contributions to the phase are discussed in the supplementary material.

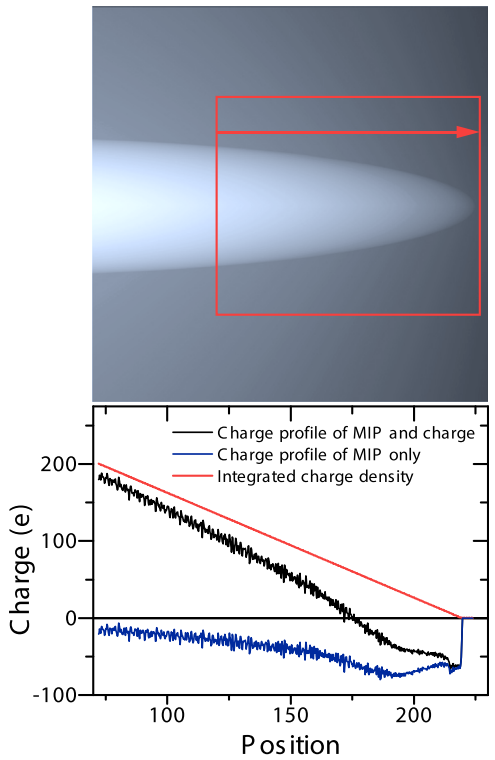

FIG. 2. Top: Simulated phase image of the end of a needle that has an ellipsoidal shape, including contributions from both the mean inner potential (MIP) and a line of constant charge density along the needle axis, according to the model described in the text. A value for the mean inner potential of 15 V was used. The red rectangle shows an integration contour, which was used to determine the charge profiles shown in the graph. The red line in the graph shows the cumulative charge along the needle, which was input into the simulation. The black and blue graphs show inferred cumulative charge profiles obtained by integrating the total phase shift shown in the phase image and only the mean inner potential contribution to the phase, respectively. The position on the horizontal axis is shown in units of nm.

B. Model-based approach

Model-based measurement of the charge density in the APT needle was performed by fitting the part of the recorded phase image that lies outside the boundary of the needle to a simulated phase image, which was generated by approximating the needle by a line of constant charge density,[18] for which an analytical solution for the phase shift takes the form

$$\begin{aligned}\phi(x,y) = C_E \frac{\sigma}{4\pi\epsilon_0} \times \Bigg\{ & -(c-y+h)\ln\sqrt{x^2+(c-y+h)^2} \\ & -(c+y-h)\ln\sqrt{x^2+(c+y-h)^2} \\ & +(c+y+h)\ln\sqrt{x^2+(c+y+h)^2} \\ & +(c-y-h)\ln\sqrt{x^2+(c-y-h)^2} \\ & -|x|\sin^{-1}\left(\frac{c-y+h}{\sqrt{x^2+(c-y+h)^2}}\right) \\ & -|x|\sin^{-1}\left(\frac{c+y-h}{\sqrt{x^2+(c+y-h)^2}}\right) \\ & +|x|\sin^{-1}\left(\frac{c+y+h}{\sqrt{x^2+(c+y+h)^2}}\right) \\ & +|x|\sin^{-1}\left(\frac{c-y-h}{\sqrt{x^2+(c-y-h)^2}}\right)\Bigg\}, \end{aligned} \tag{3}$$

where $2c$ is the length of the line charge, σ is the charge density, x and y are in-plane coordinates, and $2h$ is the distance between the electrodes,[22,25] as shown schematically in Fig. 3. A best-fitting model to a chosen experimental phase image was obtained by fitting the parameters c, h, and σ.

The linear charge density profile described by Eq. (3) was chosen because it results in ellipsoidal equipotential contours surrounding the line charge that inherently resemble the surface of the needle,[25,36–39] which is itself expected to be approximately ellipsoidal in the present study. As the model-based approach is applied to the region of the phase image that lies outside the object, it is insensitive to the mean inner potential contribution to the phase.

An important limitation of the model-based approach is that it requires *a priori* knowledge of the morphology and likely charge distribution in the specimen. It is also affected by perturbation of the vacuum reference wave,[20,21] as a result of the fact that an off-axis electron hologram is formed by overlapping a specimen electron wave with a reference wave that is affected by phase modulations associated with the electromagnetic field of the specimen itself. Here, the perturbed reference wave was taken into account in the model by rewriting the total phase shift ϕ_T in the form

$$\phi_T(x,y) = \phi(x,y) + \phi(x + x_{BP}, y), \tag{4}$$

where ϕ is defined in Eq. (3), x_{BP} is the distance between the object and reference waves (used here as an additional fitting parameter) and the biprism is assumed to be parallel to the y axis.

IV. EXPERIMENTAL RESULTS AND DISCUSSION

Both the model-independent and the model-based approach were used to determine the charge density in the Fe needle shown in Fig. 1. Figure 4(a) shows the cosine of an as-acquired phase image, in which the contributions to the phase from the mean inner potential, the applied bias and the magnetic field are all still present.

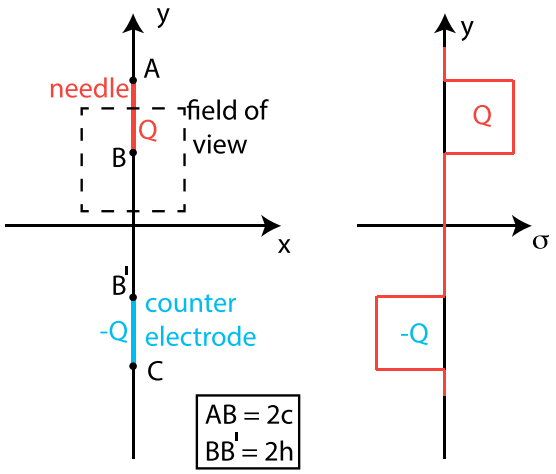

FIG. 3. Left: Schematic diagram showing the model that was used to provide a best fit to the measured phase shift outside the needle in the model-based approach. Charge segments corresponding to the atom probe needle and the counter-electrode are labeled AB and $B'C$, respectively. Right: The assumed charge density distribution along the y axis.

For the model-independent approach, the mean inner potential and magnetic contributions to the phase were subtracted by taking the difference between two phase images recorded at different applied bias voltages (e.g., 0 and 5 V). This procedure also resulted in subtraction of the contribution to the perturbed reference wave from the magnetic field of the needle. Contour integration was then applied to the image shown in Fig. 4(b). As imprecise subtraction of images would influence the measured charge density, all phase images were aligned with sub-pixel precision and no evidence of misalignment artefacts was observed. Any effects of dynamical diffraction and Fresnel fringes are assumed to be unchanged between successive images and to cancel out when pairs of phase images are acquired at different bias voltages and subtracted from each other.

The results of applying the model-based approach to obtain a best-fitting simulation *outside* the needle to the phase image in Fig. 4(b) are shown in Figs. 4(c) and 4(d), before and after taking the perturbed reference wave into account using Eq. (4), respectively. The perturbed reference wave results in slight asymmetry in the contours in Fig. 4(d), similar to that in the experimental phase contours in Fig. 4(b). Although the effect is not very pronounced in the present measurement, its inclusion improves the goodness of fit (R^2) from 0.9992 to 0.9995.

Figure 5 shows a comparison of the cumulative charge profiles measured using the two methods. The black curve in Fig. 5(a) was obtained using the model-independent

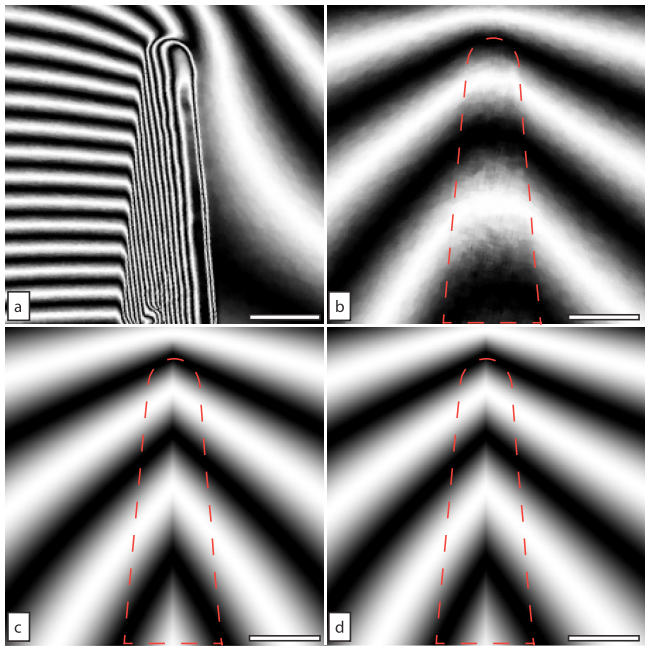

FIG. 4. (a) Experimental contoured phase image recorded from a single electron hologram of the APT needle before removing the mean inner potential and magnetic contributions to the phase. (b) Contoured phase difference image showing only the electrostatic contribution, after removing the mean inner potential and magnetic contributions to the phase. (c) Simulated contoured phase image, corresponding to a best-fitting model to (b) assuming a constant charge density along the needle axis, without including the perturbed reference wave in the simulation. (d) As for (c), but including the perturbed reference wave in the simulation as a fitting parameter. In all of the images, the electrostatic contribution corresponds to a bias voltage of 5 V applied to the needle. The phase amplification factor is 1. The scale bar is 50 nm.

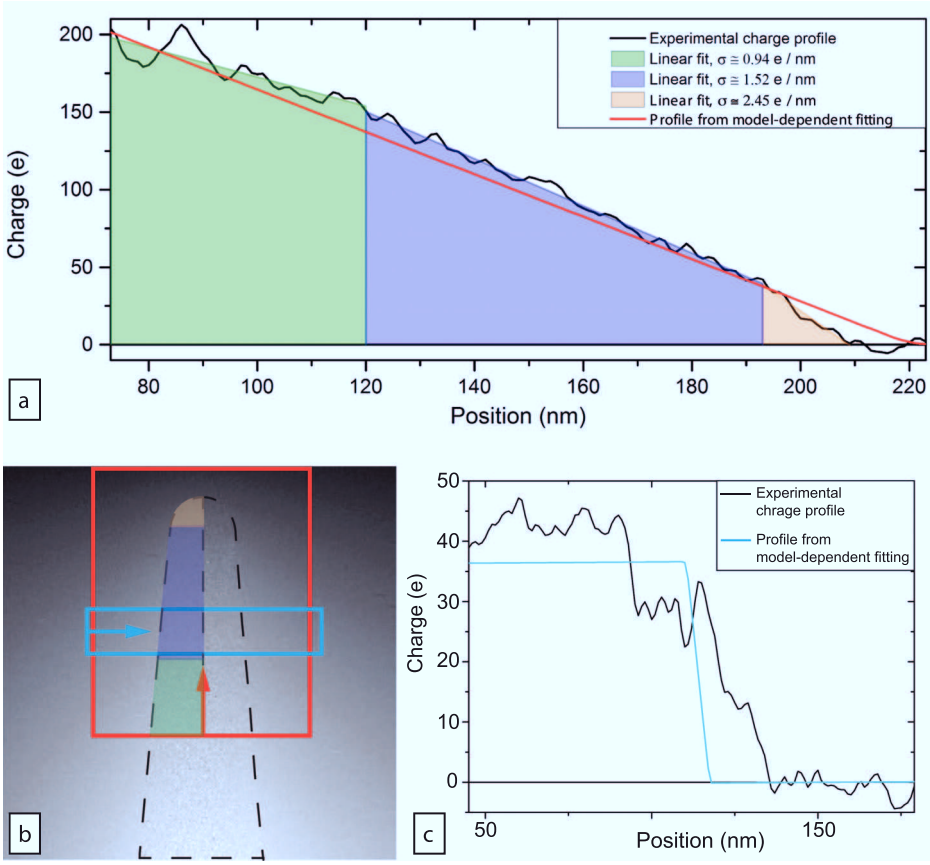

FIG. 5. (a) Cumulative charge profile measured along the electrically biased atom probe needle for an applied bias V_B of 5 V, with the counter-electrode at distance of approximately 1 μm. The black line shows the result of model-independent fitting using contour integration. The red line shows the result of model-based fitting using a line of constant charge density. (b) Reconstructed electron-optical phase after subtracting contributions from the mean inner potential and the magnetic field of the specimen. The edge of the needle is outlined with a black dashed line. The red and cyan boxes show integration contours, with the arrows indicating the directions in which the sizes of the boxes were changed. Regions marked in colour in (a) and (b) correspond to different charge densities identified from the black line profile in (a). (Only half of the tip is marked in colour in (b) to allow the phase distribution in the other half of the tip to be seen). (c) Charge profile measured across the needle using the cyan integration contour marked in (b). The black profile results from applying the model-independent contour integration approach, while the cyan profile corresponds to model-based fitting of the charge.

approach by changing the size of the red contour in the direction denoted by the red arrow in Fig. 5(b). The total amount of charge can be seen to increase on going inside the needle and, as expected, there is no charge measured outside the needle (between approximately 210 and 220 nm in the graph).

The red line, which was obtained using the model-based approach by fitting the phase *outside* the needle, agrees quantitatively with that determined using the model-independent approach across most of the graph. However, the two approaches show a discrepancy in the apex region of the needle, where the model-based fit (the red line) extends outside the needle (between 210 and 215 nm), while the profile determined using the model-independent approach shows charge accumulation (i.e., the black curve has a steeper slope than the red line between approximately 195 and 210 nm). The charge accumulation at the apex most probably results from the deviation of the apex shape from an ellipsoid. The discrepancy between the two cumulative charge profiles in Fig. 5(a) indicates that the constant charge density assumed in the model-based approach is not sufficiently accurate in the apex region. Based on the model-independent cumulative charge profile, we defined three regions that have the following charge densities: $\sim 0.94\, e^-$/nm in the shank of the needle (green); $\sim 1.52\, e^-$/nm in the middle section (blue); and $\sim 2.45\, e^-$/nm at the apex of the needle (orange).

Similar cumulative charge profiles were also measured in the perpendicular direction (across the needle), as shown in Fig. 5(c). The result of applying the model-independent approach, which is shown in black, was obtained by shrinking the integration contour shown in cyan in Fig. 5(b) in the direction of the arrow. The cumulative charge profile obtained from the model-based approach used to fit the phase outside the needle is shown in cyan in Fig. 5(c). Both methods provide consistent values for the total charge across the tip. The detailed shape of the profile obtained using the model-independent approach is difficult to interpret due to poor signal to noise, which results from the thickness of the shank of the needle in this region and the small size of the integration contour. (Such problems can be tackled in a future study by using either cumulative acquisition of electron holograms or phase-shifting electron holography). Nevertheless, it can be seen that, as expected, the charge in the needle is not concentrated on the axis of the needle, as assumed in the model-based approach, in which the charge

distribution is only used to describe the field outside the needle.

In order to obtain confidence in the results, similar cumulative charge profiles were measured from electron holograms acquired at different specimen tilt angles in the range ±45° (limited by the tilt range of the STM-TEM specimen holder). The reconstructed amplitude and phase images showed that the needle and the field surrounding it are very close to being cylindrically symmetrical (see supplementary material). A selection of the resulting charge profiles measured along the needle is shown in Fig. 6 for specimen tilt angles of −43°, +5°, +25°, and +43°. The profiles are consistent with each other to within experimental error, also indicating that subtraction of the mean inner potential contribution to the phase was not affected by slight changes in diffraction contrast between holograms acquired at different specimen tilt angles. For a non-cylindrically symmetrical object, a similar approach could, in principle, be used to measure the three-dimensional charge distribution in the specimen. It should be noted that a detailed mathematical discussion of the influence of phase noise on the measured charge density is outside the scope of the present paper. Instead, we have restricted ourselves to showing line profiles in Figs. 5(a), 5(c), and 6, which illustrate the uncertainty in the measured cumulative charge density visually.

Since the phase shift resulting from the electrostatic potential satisfies the projection requirement for electron tomography, backprojection-based or model-based reconstruction algorithms can be used to reconstruct the three-dimensional electrostatic potential distribution within and around a specimen.[2,3,40] In the present study, limitations in the available specimen tilt range to ±45° would be likely to result in pronounced artefacts in such a reconstruction.[41] Here, on the assumption of cylindrical symmetry (see Sec. III), we inferred the three-dimensional distributions of electrostatic potential and electric field around the needle from the three charge density distributions indicated in Fig. 5(a). This approach overcomes the influence of the perturbed reference wave on the recorded phase, as well as the fact that the projected potential extends outside the field of view of the recorded electron hologram.

Our calculation makes use of the fact that the electrostatic potential V associated with a line charge of constant charge density σ can be written in the form[25]

$$V(x,y,z,\sigma,c,h) = \frac{\sigma}{4\pi\epsilon_0} \times \left\{ \sinh^{-1}\left(\frac{c-y+h}{\sqrt{x^2+z^2}}\right) - \sinh^{-1}\left(\frac{-c-y+h}{\sqrt{x^2+z^2}}\right) + \sinh^{-1}\left(\frac{-c-y-h}{\sqrt{x^2+z^2}}\right) - \sinh^{-1}\left(\frac{c-y-h}{\sqrt{x^2+z^2}}\right) \right\}. \quad (5)$$

Our model then corresponds to a representation of the needle using three superimposed line charges that are centred on the same point, with the longest line corresponding to a charge density of one sign and the other two lines corresponding to charge densities of opposite sign, as shown in Fig. 7. The total electrostatic potential, which is a superposition of the potentials of the three segments (A, B, C) (see Fig. 7) corresponding to charge densities σ_1, σ_2, and σ_3 (see Fig. 5(a)), is then

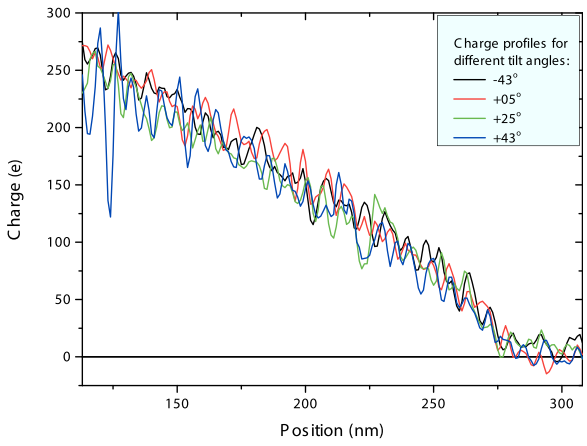

FIG. 6. Charge profile along the atom probe needle (as in Fig. 5(a)) measured using the model-independent approach for different specimen tilt angles about the needle axis (see legend).

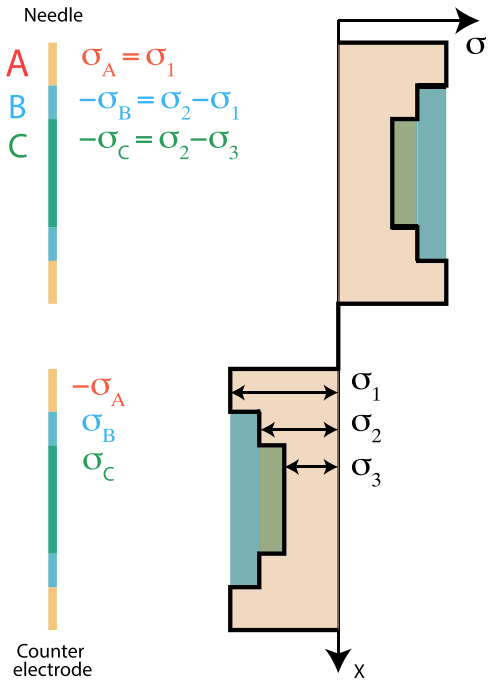

FIG. 7. Schematic diagram showing the three-charge-density model that was used to represent the charge distribution determined using the model-independent approach in Fig. 5(a) and used to create the electrostatic potential and electric field distributions shown in Fig. 8. The model is based on three superimposed line charges, which are shown schematically on the left and in the form of charge densities plotted as a function of distance on the right.

$$V_T(x,y,z) = V(x,y,z,\sigma_1,c_A,h_0) + V(x,y,z,\sigma_2-\sigma_1,c_B,h_0) + V(x,y,z,\sigma_3-\sigma_2,c_C,h_0), \quad (6)$$

where $c_A = c_0$ and h_0 are parameters determined by fitting to the experimental phase image (see above), and $2c_B$ and $2c_C$ are the lengths of segments B and C in Fig. 7 obtained from the model-independent approach.

Figure 8(a) shows a central slice taken through the resulting three-dimensional electrostatic potential and electric field distributions in the plane $z = 0$, while Fig. 8(b) shows profiles extracted from the three-dimensional electrostatic potential along the lines shown in Fig. 8(a). The profiles show the magnitude of the electrostatic potential inferred from the measured charge density distribution along the needle. When three superimposed charge densities are used (Fig. 8(a)), the equipotential contours lie close to the surface of the needle, as expected for a metallic object, with slight residual deviations of the contours from the needle's surface resulting from the fact that the needle is not a perfect ellipsoid. The electric field shown in Fig. 8(a) is fully quantitative and can be used to determine a parameter such as a field enhancement factor using an approach that is described elsewhere.[17] It should be noted that the electric field is determined from the measured charge density distribution and not directly from phase images, which would be affected by the electron holographic perturbed reference wave. Similarly, the electrostatic potential measurements shown in Figs. 8(a) and 8(b) are fully quantitative and are shown in the form of sections or line profiles through three-dimensional space and not projections. A comparison of this reconstruction with results obtained using other models discussed in this paper is presented in the supplementary material. Interestingly, the reconstructed electric field is found to be relatively insensitive to the charge distribution outside the field of view, which can be varied by changing the parameter c_0 that represents the total length of the needle, as shown in the form of simulations in the supplementary material.

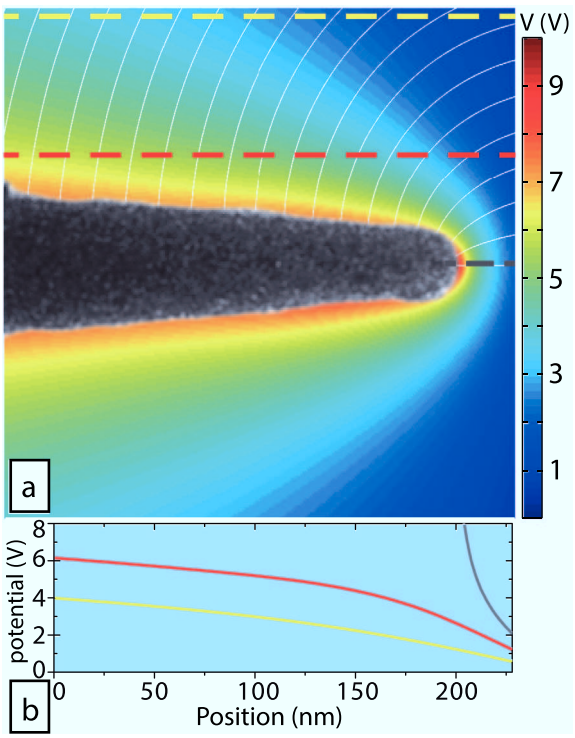

FIG. 8. (a) Central slice ($z = 0$) of the three-dimensional electrostatic potential and electric field around the atom probe needle derived from a model that utilises the three different charge densities marked in Fig. 5(a). The white lines correspond to electric field lines in the central slice, while the colours correspond to equipotential contours. The amplitude image of the needle is overlaid. (b) Line profiles of the magnitude of the electrostatic potential along the dashed lines marked in (a).

The model-independent approach that we use provides a quantitative and accurate measurement of the charge density in the needle, with no ambiguity or error, but with the precision of the measurement limited by statistical noise. The only approximation that we make comes at the stage of fitting the three different values of charge density to the measured line charge profile at the end of the needle. These three values of charge density are then used to infer the electric field and electrostatic potential around the needle on the assumption of cylindrical symmetry.

The electric field measurements described in the present study can be combined with microstructural and compositional information about APT needles obtained using other TEM techniques.[42,43] In principle, the methods that we describe can be extended to study the effect on the electric field of the presence of dielectric regions embedded in the needle.[11,26] Such studies may require the use of tilt series of electron holograms combined with inverse modelling[44] and may find future applications in studies that combine APT and TEM within the broader materials characterisation toolbox.[45,46]

V. CONCLUSIONS

We have shown how the charge distribution along an Fe atom probe needle can be measured, using either a model-independent or a model-based approach, from an electron-optical phase image recorded using off-axis electron holography in the TEM. The model-independent approach requires careful subtraction of the mean inner potential and magnetic contributions to the recorded phase shift. This subtraction was achieved by applying different bias voltages to the specimen and taking differences between the resulting phase images. The application of the model-independent approach provided a measurement of the charge inside the atom probe needle and revealed the presence of charge accumulation at its apex. The results were found to be consistent with those obtained using a model-based approach that involves fitting the phase shift associated with a line of constant charge density to the experimental phase outside the boundary of the needle. On the assumption of cylindrical symmetry, the measured charge distribution was used to determine the three-dimensional electric field and electrostatic potential outside the needle with ~10 nm spatial resolution, without needing to consider either the influence of the perturbed reference wave or the extension of the projected potential outside the field of view of the electron hologram.

ACKNOWLEDGMENTS

We are grateful to J. Caron for help with implementation of the contour integration algorithm. We also thank G. Pozzi

and C. Dwyer for fruitful discussions. R.D.B. acknowledges the European Commission for an Advanced Grant and the Deutsche Forschungsgemeinschaft for a Deutsch-Israelische Projektkooperation (DIP) Grant. V.M. and R.D.B. acknowledge the European Commission project SIMDALEE2: Marie Curie Initial Training Network (ITN) Grant No. 606988 under FP7-PEOPLE-2013-ITN.

[1]M. R. McCartney, M. A. Gribelyuk, J. Li, P. Ronsheim, J. S. McMurray, and D. J. Smith, Appl. Phys. Lett. **80**, 3213 (2002).
[2]A. C. Twitchett-Harrison, T. J. V. Yates, R. E. Dunin-Borkowski, and P. A. Midgley, Ultramicroscopy **108**, 1401 (2008).
[3]D. Wolf, A. Lubk, F. Räder, and H. Lichte, Curr. Opin. Solid State Mater. Sci. **17**, 126 (2013).
[4]D. Wolf, A. Lubk, A. Lenk, S. Sturm, and H. Lichte, Appl. Phys. Lett. **103**, 264104 (2013).
[5]K. Hata, A. Takakura, K. Miura, A. Ohshita, and Y. Saito, J. Vac. Sci. Technol., B **22**, 1312 (2004).
[6]T. Oikawa, J. J. Kim, T. Tomita, H. S. Park, and D. Shindo, J. Electron Microsc. **56**, 171 (2007).
[7]S. Darbari, Y. Abdi, S. Mohajerzadeh, and E. A. Soleimani, Carbon **48**, 2493 (2010).
[8]Y.-M. Chang, M.-L. Lin, T.-Y. Lai, H.-Y. Lee, C.-M. Lin, Y.-C. S. Wu, and J.-Y. Juang, ACS Appl. Mater. Interfaces **4**, 6676 (2012).
[9]M. K. Miller, *Atom Probe Tomography: Analysis at the Atomic Level* (Kluwer Academic/Plenum Publishers, New York, 2000).
[10]T. F. Kelly and M. K. Miller, Rev. Sci. Instrum. **78**, 031101 (2007).
[11]C. Oberdorfer and G. Schmitz, Microsc. Microanal. **17**, 15 (2011).
[12]F. Vurpillot, A. Bostel, and D. Blavette, Appl. Phys. Lett. **76**, 3127 (2000).
[13]C. Hatzoglou, B. Radiguet, and P. Pareige, in *2nd Meeting of the JTT: Nuclear Fe Alloys: Modelling and Experiments (Nuclear FAME), Universite Rouen, France, May 2012*.
[14]G. F. Missiroli, G. Pozzi, and U. Valdre, J. Phys. E: Sci. Instrum. **14**, 649 (1981).
[15]A. Tonomura, *Electron Holography*, 2nd ed., Springer Series in Optical Sciences (Springer, 1999).
[16]H. Lichte and M. Lehmann, Rep. Prog. Phys. **71**, 016102 (2008).
[17]M. Beleggia, T. Kasama, D. J. Larson, T. F. Kelly, R. E. Dunin-Borkowski, and G. Pozzi, J. Appl. Phys. **116**, 024305 (2014).
[18]M. Beleggia, T. Kasama, R. E. Dunin-Borkowski, S. Hofmann, and G. Pozzi, Appl. Phys. Lett. **98**, 243101 (2011).
[19]D. Van Dyck, J. Electron Microsc. **48**, 33 (1999).
[20]G. Matteucci, G. F. Missiroli, E. Nichelatti, A. Migliori, M. Vanzi, and G. Pozzi, J. Appl. Phys. **69**, 1835 (1991).
[21]G. Matteucci, G. F. Missiroli, and G. Pozzi, *Electron Microscopy and Holography II*, Advances in Imaging and Electron Physics Vol. 122, edited by P. W. Hawkes (Elsevier, 2002), pp. 173–249.
[22]G. Pozzi, M. Beleggia, T. Kasama, and R. E. Dunin-Borkowski, C. R. Phys. **15**, 126 (2014).
[23]C. Gatel, A. Lubk, G. Pozzi, E. Snoeck, and M. Hýtch, Phys. Rev. Lett. **111**, 025501 (2013).
[24]N. Ikarashi, K. Kaneko, M. Saitoh, and H. Takeda, Jpn. J. Appl. Phys., Part 1 **53**, 031101 (2014).
[25]G. Matteucci, G. Missiroli, M. Muccini, and G. Pozzi, Ultramicroscopy **45**, 77 (1992).
[26]M. K. Miller, T. F. Kelly, K. Rajan, and S. P. Ringer, Mater. Today **15**, 158 (2012).
[27]D. Gabor, Nature **161**, 777 (1948).
[28]R. E. Dunin-Borkowski, Ultramicroscopy **83**, 193 (2000).
[29]A. C. Twitchett, R. E. Dunin-Borkowski, and P. A. Midgley, Philos. Mag. **86**, 5805 (2006).
[30]M. J. Humphry, B. Kraus, A. C. Hurst, A. M. Maiden, and J. M. Rodenburg, Nat. Commun. **3**, 730 (2012).
[31]N. Dekkers and H. de Lang, Optik **41**, 452 (1974).
[32]K. Svensson, Y. Jompol, H. Olin, and E. Olsson, Rev. Sci. Instrum. **74**, 4945 (2003).
[33]See supplementary material at http://dx.doi.org/10.1063/1.4916609 for additional information on charge measurement in the APT needle.
[34]M. R. McCartney and D. J. Smith, Annu. Rev. Mater. Res. **37**, 729 (2007).
[35]M. O'Keeffe and J. C. H. Spence, Acta Crystallogr. A **50**, 33 (1994).
[36]E. Durand, *Électrostatique* (Masson, Paris, 1964), Vol. 2.
[37]L. D. Landau and E. Lifshitz, *Theoretical Physics. Electrodynamics of Continuous Media*, 2nd ed. (Nauka, Moscow, 1982), Vol. 8.
[38]G. Matteucci, G. F. Missiroli, and G. Pozzi, J. Electron Microsc. **45**, 27 (1996).
[39]R. J. Rowley, Am. J. Phys. **74**, 1120 (2006).
[40]G. Lai, T. Hirayama, K. Ishizuka, T. Tanji, and A. Tonomura, Appl. Opt. **33**, 829 (1994).
[41]A. Alpers, R. J. Gardner, S. König, R. S. Pennington, C. B. Boothroyd, L. Houben, R. E. Dunin-Borkowski, and K. J. Batenburg, Ultramicroscopy **128**, 42 (2013).
[42]I. Arslan, E. A. Marquis, M. Homer, M. A. Hekmaty, and N. C. Bartelt, Ultramicroscopy **108**, 1579 (2008).
[43]A. J. Detor, M. K. Miller, and C. A. Schuh, Philos. Mag. **86**, 4459 (2006).
[44]J. Caron, J. Ungermann, R. E. Dunin-Borkowski, and M. Riese, in *Proceedings of the 18th International Microscopy Congress, Prague, Czech Republic, 7–12 September 2014*, IT-11-O-2781.
[45]M. K. Miller and T. F. Kelly, Microsc. Microanal. **16**, 1856 (2010).
[46]I. M. Robertson, C. A. Schuh, J. S. Vetrano, N. D. Browning, D. P. Field, D. J. Jensen, M. K. Miller, I. Baker, D. C. Dunand, R. E. Dunin-Borkowski, B. Kabius, T. F. Kelly, S. Lozano-Perez, A. Misra, G. S. Rohrer, A. D. Rollett, M. L. Taheri, G. B. Thompson, M. Uchic, X.-L. Wang, and G. Was, J. Mater. Res. **26**, 1341 (2011).